



3-D crustal and uppermost mantle structure beneath NE China revealed by ambient noise adjoint tomography

Yanling Liu^{a,b}, Fenglin Niu^{c,b,*}, Min Chen^b, Wencai Yang^a

^a Key Laboratory of Geo-Detection Ministry of Education, and School of Geophysics and Information Technology, China University of Geosciences (Beijing), Beijing, 100083, China

^b Department of Earth Science, Rice University, Houston, TX 77005, USA

^c State Key Laboratory of Petroleum Resources and Prospecting, and Unconventional Natural Gas Institute, China University of Petroleum at Beijing, Beijing, 102249, China

ARTICLE INFO

Article history:

Received 27 July 2016

Received in revised form 18 December 2016

Accepted 20 December 2016

Available online 5 January 2017

Editor: P. Shearer

Keywords:

Northeast China
empirical Green's function
adjoint tomography
low wave speed conduit
partial melting
Cenozoic volcanism

ABSTRACT

We construct a new 3-D shear wave speed model of the crust and the uppermost mantle beneath Northeast China using the ambient noise adjoint tomography method. Without intermediate steps of measuring phase dispersion, the adjoint tomography inverts for shear wave speeds of the crust and uppermost mantle directly from 6–40 s waveforms of Empirical Green's functions (EGFs) of Rayleigh waves, which are derived from interferometry of two years of ambient noise data recorded by the 127 Northeast China Extended Seismic Array stations. With an initial 3-D model derived from traditional asymptotic surface wave tomography method, adjoint tomography refines the 3-D model by iteratively minimizing the frequency-dependent traveltimes misfits between EGFs and synthetic Green's functions measured in four period bands: 6–15 s, 10–20 s, 15–30 s, and 20–40 s. Our new model shows shear wave speed anomalies that are spatially correlated with known tectonic units such as the Great Xing'an range and the Changbaishan mountain range. The new model also reveals low wave speed conduits in the mid-lower crust and the uppermost mantle with a wave speed reduction indicative of partial melting beneath the Halaha, Xilinhote–Abaga, and Jingpohu volcanic complexes, suggesting that the Cenozoic volcanism in the area has a deep origin. Overall, the adjoint tomographic images show more vertically continuous velocity anomalies with larger amplitudes due to the consideration of the finite frequency and 3-D effects.

© 2016 Elsevier B.V. All rights reserved.

1. Introduction

Northeast China (NE China) is bounded by two distinct cratons, the North China craton in the south and the Siberia craton in the north, and stretches to the Japan Sea in the east. NE China consists mainly of two composite blocks, the Songnen–Jiamusi and Erguna–Great Xing'an, which completed the accretion in Early Permian (Klimetz, 1983; Meng, 2003; Li, 2006; Li et al., 2012; Zhou and Wilde, 2013). It then collided with the North China craton along its southern edge after the closure of the Paleo-Asian Ocean in the Late Permian to Early Triassic (Eizenhofer et al., 2014), followed by a second collision with the Siberia craton along the northern edge after the closure of the Mongol–Okhotsk Ocean in the Late Jurassic to Early Cretaceous times (Van der Voo et al., 2015). These two collisions led to the formation of

the Solonker suture zone in the south and the Mongol–Okhotsk suture zone in the north (Fig. 1). During and after these collisions, NE China experiences a series of orogeny, basin formation and volcanism (Li and Ouyang, 1998; Ge et al., 2010; Lin, 2011; Tang et al., 2014), and now the region has evolved to a mosaic of several distinct terranes, including orogenic belts, basins and volcanoes. We divide NE China into three main tectonic units, the Great Xing'an range (also known as the Xing'an–Mongolia Orogenic Belt, XMOB) in the west, the Songliao basin in the middle, and the Changbaishan–Jingpohu range in the east (Fig. 1).

The Great Xing'an range is the eastern part of the Central Asian Orogenic Belt (CAOB), which is also known as the Altaids and is one of the largest accretionary orogens in the world developed between ~600 Ma and 250 Ma by multiple accretions of terranes with different origins (Shao et al., 1994; Li and Ouyang, 1998; Wilhem et al., 2012; Zhou and Wilde, 2013). The NNE trending Daxing'anling–Taihang Gravity Line (DTGL) (Xu, 2006) separates the Great Xing'an range from the Songliao basin. The Songliao basin, located at the center of our study area, is a rift basin, and the rifting process took place in Mesozoic (Hu et al., 1998;

* Corresponding author at: State Key Laboratory of Petroleum Resources and Prospecting, and Unconventional Natural Gas Institute, China University of Petroleum at Beijing, Beijing, 102249, China.

E-mail address: niu@cup.edu.cn (F. Niu).

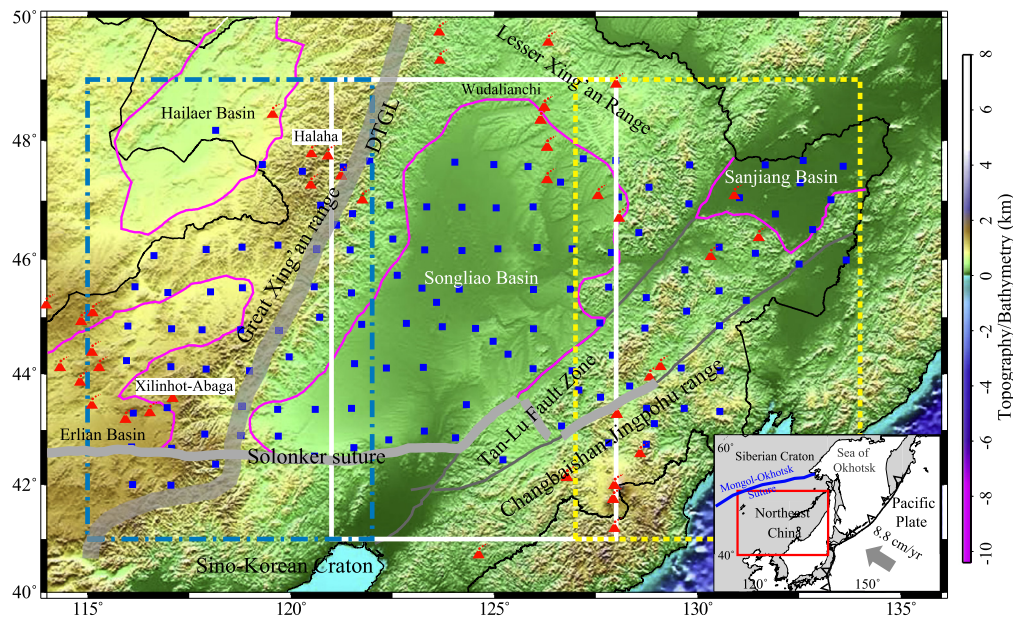


Fig. 1. Map showing topography, major geological features and distribution of the broadband NECESSArray stations in NE China. The magenta lines outline major basins in the area. The thin dark gray solid lines represent the two branches of the Tan-Lu Fault Zone in the area. The medium thick gray line indicates the Solonker suture zone, and the thick gray line labeled as DTGL indicates the Daxing'anling–Taihang Gravity Line. The blue squares mark NECESSArray stations. Locations of three simulation domains are outlined by blue dash-dotted, white solid, and yellow dotted boxes, respectively. Red volcanic symbols show the major Cenozoic volcanism in the area. Inset shows the motion of the Pacific plate relative to the Eurasian plate. (For interpretation of the references to color in this figure legend, the reader is referred to the web version of this article.)

Feng et al., 2010; Ge et al., 2010) right after the closure of the Mongol–Okhotsk Ocean. Late Mesozoic volcanic rocks are widely distributed in the region, indicating active volcanism occurred during the Mesozoic rifting.

Volcanism continued in the Cenozoic time but was rather episodic and sporadic, which shows a spatial shift from the center of the Songliao basin to the edges of the basin in Early Miocene (Liu et al., 2001), coinciding with the onset of the Japan Sea opening. Late Cenozoic volcanoes around the Songliao basin include the Changbaishan, Jingpohu, Wudalianchi, Halaha, and Xilinhót–Abaga from the southeast to the southwest. Located next to the southeastern corner of the Songliao basin, the Changbaishan–Jingpohu range marks the boundary between China and North Korea and hosts the largest active volcano (the Changbaishan volcano) in NE China. The Changbaishan volcano (also known as Baitoushan volcano in North Korea) has had a series of eruptions since ~2.77 Ma (Wang et al., 2003) and the latest eruption occurred in 1702. On the other hand, both the Halaha and the Xilinhót–Abaga volcanic groups sit on the Great Xing'an range, located to the west side of the DTGL (Fan et al., 2015). The Halaha volcanic group situates in the northern part of the range and consists of tens of Quaternary volcanoes that overlie Jurassic intrusive rocks with a peak formation time around ~135–145 Ma (Wang et al., 2006; Fan et al., 2015). The Xilinhót–Abaga volcanic group in the south comprises more than 300 volcanoes and a lava plateau spreading over an area of more than 10,000 km² (Wang et al., 2006; Chen et al., 2015; Fan et al., 2015).

Geochemical studies of the Cenozoic volcanoes from NE China (e.g., Zou et al., 2008; Chen et al., 2015; Guo et al., 2016a) indicate that the intraplate alkaline basalts have isotopic signatures close to those of the present-day ocean island basalts (OIBs), suggesting that they have a deep origin in the asthenosphere. The NE China magmatism has been attributed to upwelling of warm hydrated mantle from the top of the stagnant slab (e.g., Lei and Zhao, 2005; Zhao et al., 2008; Chen et al., 2015; Guo et al., 2016a). This idea is largely based on tomography models showing flat slabs (high wave speeds) in the transition zone beneath NE China volcanoes with slow shallow mantle wave speeds above. Tang et al. (2014)

propose a different mechanism causing the Changbaishan volcanism, which invokes decompression melting of a warm and buoyant upwelling rising through a gap in the deep stagnant slab. The upwelling originates from the asthenosphere that used to be beneath the Pacific and was contaminated by plumes and became superadiabatic. It was then trapped beneath the subducting Pacific plate and transported to greater depths. For the Halaha and Xilinhót–Abaga volcanoes, Guo et al. (2016b) attribute them to mantle upwellings generated by return flows of a downwelling beneath the Songliao basin.

Both body and surface wave tomography studies show low wave speed anomalies (LV) in the upper mantle beneath the Changbaishan, Halaha, and Xilinhót–Abaga volcanic regions (Tang et al., 2014; Guo et al., 2016b; Kang et al., 2016). The amplitude of the LVs beneath the Halaha and Xilinhót–Abaga regions are not so strong and there are no significant low wave speed anomalies within the crust. The low amplitude of LV in the upper mantle and the lack of the LV in the crust are likely to be caused by tomographic errors from wavefront healing (e.g., Hung et al., 2001; Malcolm and Trampert, 2011), because both the body (Tang et al., 2014) and surface wave tomography studies (Guo et al., 2016b) employ 1-D reference models and invert either the traveltime or dispersion data by assuming 1-D great-circle propagation paths. Recently, Huang et al. (2015) found a strong low wave speed zone in the lower crust beneath the Yellowstone supervolcano, which they interpreted as a basaltic magma body with ~2% of melt. Thus obtaining more accurate absolute wave speeds to quantify melt fraction and magma structure in the lower crust and upper mantle beneath the Halaha and Xilinhót–Abaga volcanoes are essential to understand the magmatism of the Great Xing'an range.

Surface wave data obtained from teleseismic earthquakes and ambient noise have the ability to resolve structures of the lower crust and upper mantle. In our study area, Guo et al. (2015, 2016b) conducted surface wave tomography using both ambient noise and earthquake data, and the resulting 3-D S-wave model shows a large wave speed contrast between the Songliao basin and the Great Xing'an range. Li et al. (2016) incorporated Rayleigh wave ellipticity, i.e. Rayleigh-wave Z/H (vertical to horizontal) amplitude

ratio, in the dispersion inversion, which resulted better images of the upper crustal wave speed structure of the area. These studies, however, employed the so-called traditional surface wave tomographic approach, which requires constructing phase (or group) velocity maps by assuming a great circle raypath and a 1-D layered wave speed model in inverting the phase velocities at each grid. Both assumptions affect the inverted 3-D wave speed structure and especially lead to underestimating the amplitude of low wave speed anomalies. To overcome the limitations of these two assumptions, [Chen et al. \(2014\)](#) proposed the ambient noise adjoint tomography technique that formulates the inversion by a direct matching of the ambient noise derived surface-wave waveforms with 3-D synthetics calculated based on a spectral-element method (SEM) ([Komatitsch and Tromp, 2002a, 2002b; Komatitsch et al., 2004](#)).

In order to better image the crustal and uppermost mantle wave speed structure of the NE China, we applied the ambient noise adjoint tomography ([Chen et al., 2014](#)) on a data set of Rayleigh wave empirical Green's functions (EGFs), derived from ambient noise interferometry of 127 NECESSArray (NorthEast China Extended Seismic Array) stations. We present a refined 3-D model of the crust and uppermost mantle beneath NE China. We focus on discussing the new seismic features in the model and their implications to the origin of the widespread volcanism and the tectonic evolution of NE China.

2. NECESSArray data

We use the continuous data recorded by the NECESSArray, which consists of 127 temporary stations (blue squares in [Fig. 1](#)). The 127 temporal stations were deployed under an international collaboration among China, Japan and US in NE China between September of 2009 and August of 2011. The array covers an area of 116°E–134°E and 41.5°N–49.0°N, roughly ~1800 km and ~800 km in the E–W and N–S direction, respectively ([Fig. 1](#)). The goal of the NECESSArray project is to build high-resolution seismic images of the crust and the mantle beneath NE China to better constrain the subduction geometry of the Pacific plate and to better understand the large-scale extension and widespread magmatism in the area.

The noise cross-correlation functions (NCFs) are obtained in a previous tomographic study ([Guo et al., 2015](#)). Here we summarize the details in processing ambient noise data. **The standard ambient-noise cross-correlation techniques** ([Bensen et al., 2007](#)) are employed to process the vertical component of the selected stations. The continuous records of ground velocity are first decimated to a sampling rate of 5 Hz, cut into daily segments. Since the 127 stations are equipped with different types of sensors and digitizers, these daily segments are deconvolved with the corresponding instrument responses and further converted from the velocity records to displacement sequences. This step is necessary in order to effectively and correctly computing the noise cross-correlation functions (NCFs) using data recorded with different types of seismometers. A running time-window method is then applied to compute the NCFs with the daily records. The length of the running windows is taken from 409.6 s (2048 points) to 1638.4 s (8192 points) depending on the inter-station distance. Half of the running window length is set as the running step. If a gap is present within the running window in one of the two seismograms, the NCF of that time window is not computed. For each time window, the linear trend and mean are removed from the seismograms. Their Fourier transforms are further performed to compute the NCFs in the frequency domain. The spectral whitening technique is applied in order to enhance the ambient noise signals, in which the two amplitude spectra are reset to 1 in the frequency range of 0.01 Hz–1.0 Hz and to 0 elsewhere while the

phase spectra are kept unchanged. The NCFs of each running window are subsequently stacked to create a daily NCF of a station pair. All the daily NCFs are then stacked at each station pair to enhance the signal-to-noise ratio (SNR) of the Rayleigh wave arrival. The positive and negative sides of stacked NCFs are further folded and summed to obtain the final NCFs.

In this study we compute the displacement EGFs from the final NCFs using the following equation:

$$\hat{G}_{AB}(t) = -\frac{dC_{AB}(t)}{dt} \approx G_{AB} \quad (1)$$

Here $C_{AB}(t)$, $G_{AB}(t)$, and $\hat{G}_{AB}(t)$ are the noise cross-correlation function, the real Green's function and the empirical Green's function, respectively. [Fig. 2](#) shows an example of the EGFs computed at the station NE21 in different period bands. The above empirical relation reveals that the time derivative of NCF can be equivalent of EGF, which serves as an approximation of the exact Green's function, subject to frequency-dependent amplitude correction ([Weaver and Lobkis, 2004; Roux et al., 2005](#)) and errors due to, for instance, uneven source distribution of ambient noise sources ([Yao and van der Hilst, 2009; Harmon et al., 2010](#)).

3. Ambient noise adjoint tomography

We adopt the technique developed by [Chen et al. \(2014\)](#) to invert shear wave speed using ambient noise data. Here we briefly review the ambient noise adjoint tomography method. A single vertical force is set at 1 km depth beneath each station as the virtual source to generate 3-D synthetic Green's functions (SGFs), which are computed by the spectral-element code (SPECFEM3D-Cartesian) ([Komatitsch et al., 2004](#)) using a Gaussian source time function with a half duration of $T_h = 1.5$ s. The high corner frequency of a Gaussian source time function is roughly $1/4T_h$, which converts to a low corner period of 6 s, the low end of 6–40 s period band used in our inversion. An isotropic initial model ([Guo et al., 2015](#)) parameterized on the SEM Gauss–Lobatto–Legendre (GLL) integration points is used in the inversion.

An iterative approach is employed to refine the initial model to minimize the overall traveltime misfit, χ , which is the sum of the frequency-dependent traveltime misfits measured in several period bands:

$$\chi = \frac{1}{N} \sum_{i=1}^N \frac{1}{M_i} \sum_{j=1}^{M_i} \int \left(\frac{\Delta T_j(\omega)}{\sigma_j(\omega)} \right)^2 d\omega, \quad (2)$$

where N is the number of period bands, which is 4 in this study, M_i is the total number of misfit measurements in the i -th period band. $\Delta T_j(\omega)$ and $\sigma_j(\omega)$ are the traveltime misfit and its uncertainty estimated from the j -th EGFs at frequency ω in the i -th period band. We employed the multitaper method proposed by [Zhou et al. \(2004\)](#) to measure $\Delta T_j(\omega)$ and $\sigma_j(\omega)$, which are measured from the frequency response function $H_j(\omega)$ of a system that transfers from a synthetic seismogram $S_j(\omega)$ to the observed data $D_j(\omega)$, i.e. $H_j(\omega) = D_j(\omega)/S_j(\omega)$. Therefore the frequency-dependent traveltime misfit, $\Delta T_j(\omega)$, can be estimated from the phase spectrum of the frequency response function $H_j(\omega)$, which was estimated with the multitaper method. We employed 5 tapers in the estimation and the uncertainty $\sigma_j(\omega)$ was estimated with the jackknife method.

Changes in the overall traveltime misfit, $\delta\chi$, can be expressed as change in density (ρ), shear wave speed (V_S), and bulk sound speed (V_C):

$$\delta\chi = \int (K_\rho \delta \ln \rho + K_{V_S} \delta \ln V_S + K_{V_C} \delta \ln V_C) d^3\mathbf{x}, \quad (3)$$

where K_ρ , K_{V_S} , and K_{V_C} are the Fréchet derivatives with respect to ρ , V_S , and V_C .

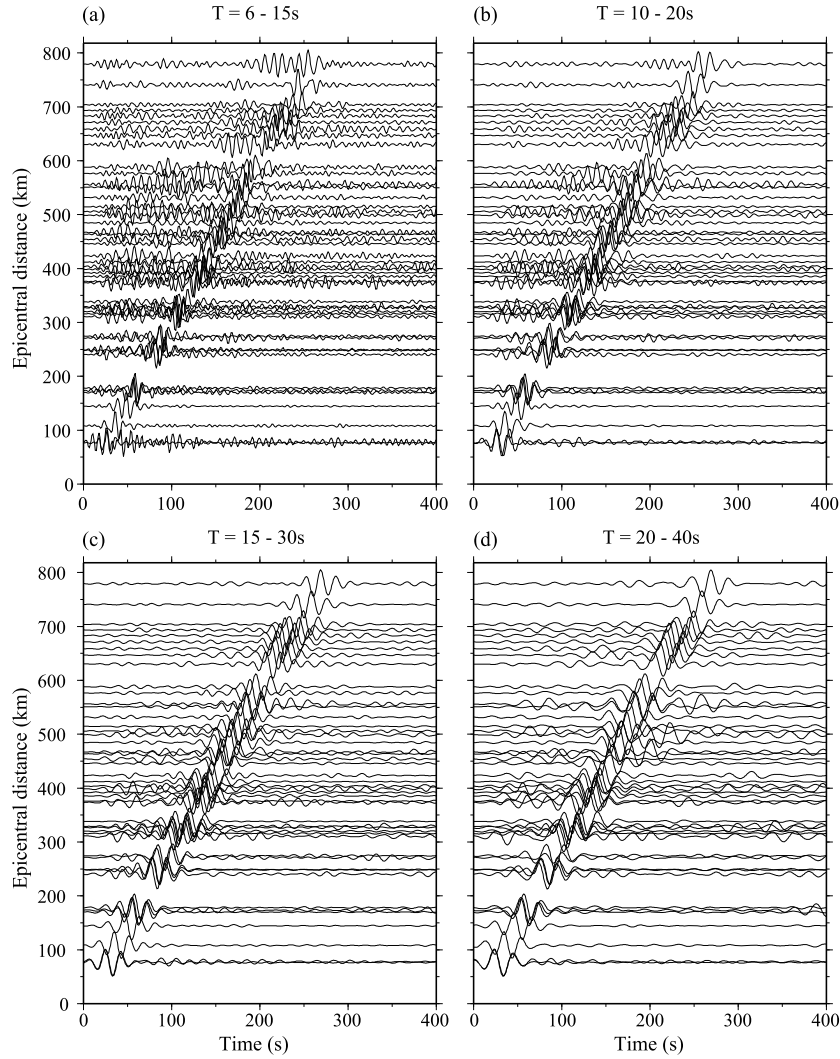


Fig. 2. Empirical Green's function waveforms derived from ambient noise interferometry between station NE21 (show in Fig. 4b) and the other stations in four different period ranges, (a) 6–15 s, (b) 10–20 s, (c) 15–30 s and (d) 20–40 s, plotted with increasing epicentral distances.

Adjoint sources are constructed from the time derivative of the time reversed SGFs weighted by the traveltimes misfit. For each virtual source station, one adjoint simulation is performed by simultaneously sending back adjoint sources at all virtual receiver stations into the 3-D model. This creates an adjoint wavefield \mathbf{s}^\dagger . The time integration of the interaction of \mathbf{s}^\dagger and the forward wavefield \mathbf{s} yields the event sensitivity kernels, which illuminate the sensitivity region of the structural parameters, ρ , V_S , and V_C .

Once all the Fréchet derivatives related to all the virtual sources are computed, we sum them and smooth the summed kernels with a Gaussian width of 40 km in the horizontal plane and 10 km in the vertical plane, then precondition the smoothed kernels (Luo, 2012) to obtain Fréchet kernel \mathbf{g} , which is the gradient of the misfit in the model space. For the k -th iteration, the model is updated by the following equation:

$$\mathbf{m}^k = \mathbf{m}^{k-1} + \alpha \mathbf{g}. \quad (4)$$

Here α is the step length, which is a positive number. \mathbf{m}^{k-1} and \mathbf{m}^k are the wave speed models before and after k -th iteration. The optimal step length is determined by minimizing the misfit calculated from a subset of virtual sources when the number of stations is large. In our case, however, since there are only ~ 40 – 45 stations in each simulation domain, thus we just use all the stations in searching for the optimal step length. Fig. 3a shows an example

of the search for the optimal step length in the western simulation domain, which has a total of 43 stations.

We exclude the density kernels in this study, because the ambient noise data are not very sensitive to density perturbations. Instead we scale the density perturbations to shear wave speed perturbations by a factor of 0.33, i.e., $\delta \ln \rho / \delta \ln V_S = 0.33$ (Panning and Romanowicz, 2006).

Our study region spans from 115°E to 134°E across the longitude and 41°N to 49°N along the latitude. In order to use SPEC-FEM3D_Cartesian software package (www.geodynamics.org) to calculate SGFs in UTM zone projected coordinates based on spectral-element method (SEM), we divide our study region into three simulation domains ($7^\circ \times 8^\circ$ in longitude and latitude, respectively) with different longitudinal ranges, 115° – 122°E , 121° – 128°E , and 127° – 134°E , which are shown with the blue, white and yellow boxes, respectively, in Fig. 1. Each simulation domain has a one-degree overlapping with the neighboring simulation domains to ensure proper stitching for a more coherent seismic model of the whole study region.

In each simulation domain, we parameterize the model parameters, ρ , V_S , and V_C at SEM GLL points with approximately 2.5 km spacing in both horizontal and vertical directions (Chen et al., 2014). The SEM mesh also accommodated the surface topography (GTOPO30 from lta.cr.usgs.gov), and extended to 100 km deep below the sea level.

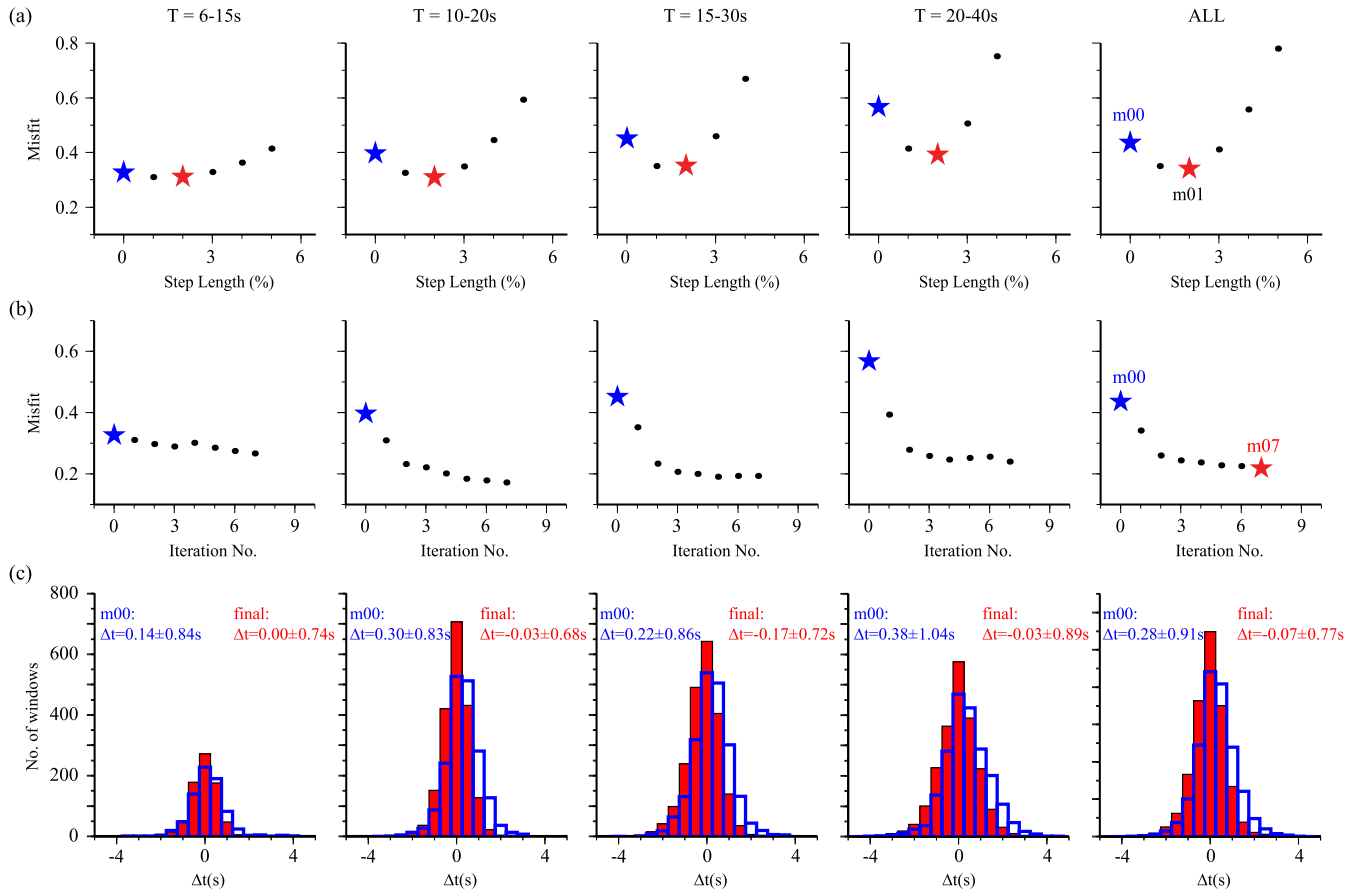


Fig. 3. (a) Line search for updating the model from M00 (blue star) to M01 (red star) for the west simulation domain. (b) Corresponding misfit evolution for the west simulation domain from M00 to M07. (c) Histograms comparison for traveltime misfits for M00 (open blue line) and the final model after 7 iterations (red bars). (For interpretation of the references to color in this figure legend, the reader is referred to the web version of this article.)

Table 1
Number of EGFs used in the inversion.

Period (s)	West	Central	East	Total
6–15	324	180	256	760
10–20	715	716	488	1919
15–30	804	786	514	2014
20–40	786	788	500	2074
ALL	2629	2470	1758	6857

We filter the EGFs and SGFs in four period bands: 6–15 s, 10–20 s, 15–30 s, and 20–40 s. Examples of the filtered EGFs in different period bands are shown in Fig. 2. In each period band, we select the traveltime misfit measurement windows using the FLEXWIN algorithm developed by Maggi et al. (2009). For each selected window, we measure the frequency-dependent traveltime misfits between EGFs and SGFs using the multi-taper method (Zhou et al., 2004). Perturbations of the shear wave and bulk sound wave speeds, V_S and V_C , are linked to the SGF-EGF traveltime misfit, χ , through equations (2) and (3) (Tromp et al., 2005). By minimizing χ iteratively, we seek for improving the model by perturbing the structural parameters. Table 1 lists the number of EGFs in the three regions that are selected from the four period bands used in the inversion.

Our starting model is taken from the result from Guo et al. (2015), which provides primarily a V_S model of NE China, and we derive the V_P and ρ values according to their model description (Guo et al., 2015). The initial SGFs and EGFs have reasonably good fits but show certain misfits in phase in different period bands. The misfit seems to increase with increasing period (Fig. 3c). Following

the steps described above, we repeat the inversion procedures iteratively until no significant further reduction of χ is shown, which in our case occurs after 4–7 iterations for each of the three simulation domains. Fig. 3b shows an example of misfit reduction with increasing number of iteration for the simulation domain in the west. The final 3D model for this simulation domain shows a significant reduction in the misfit between the SGF and EGF (Fig. 3b). Overall, the traveltime residual drops from the initial 0.28 ± 0.91 s to the final 0.07 ± 0.77 s (Fig. 3c).

As noted above, there are two overlap areas of 1-degree wide where two sets of final model parameters derived from the inversions of partially overlapping simulation domains. We find that the discrepancies between the two final models are rather minor, usually is less than 0.5%, so we simply take the averages of the two models, and integrate them with those of the non-overlapping areas to obtain the final model of the entire study area.

4. Results and discussion

In general, Rayleigh wave phase/group velocity is less sensitive to the P-wave speed than to the S-wave speed. Also the P-wave sensitivity tends to lean more on shallow structure than the S-wave sensitivity, for example, based on Xing et al. (2016), the phase velocity for a 20-s Rayleigh wave is sensitive to the S-wave speed down to 40 km, while its P-wave speed sensitivity seems to be limited within the top 20 km. Overall, we found that the updates on the P-wave speed are less significant than the S-wave speed, and most of the velocity changes are confined within the crust. In other words, we expected that the inverted S-wave speed is more robust than the P-wave speed, which could depend largely

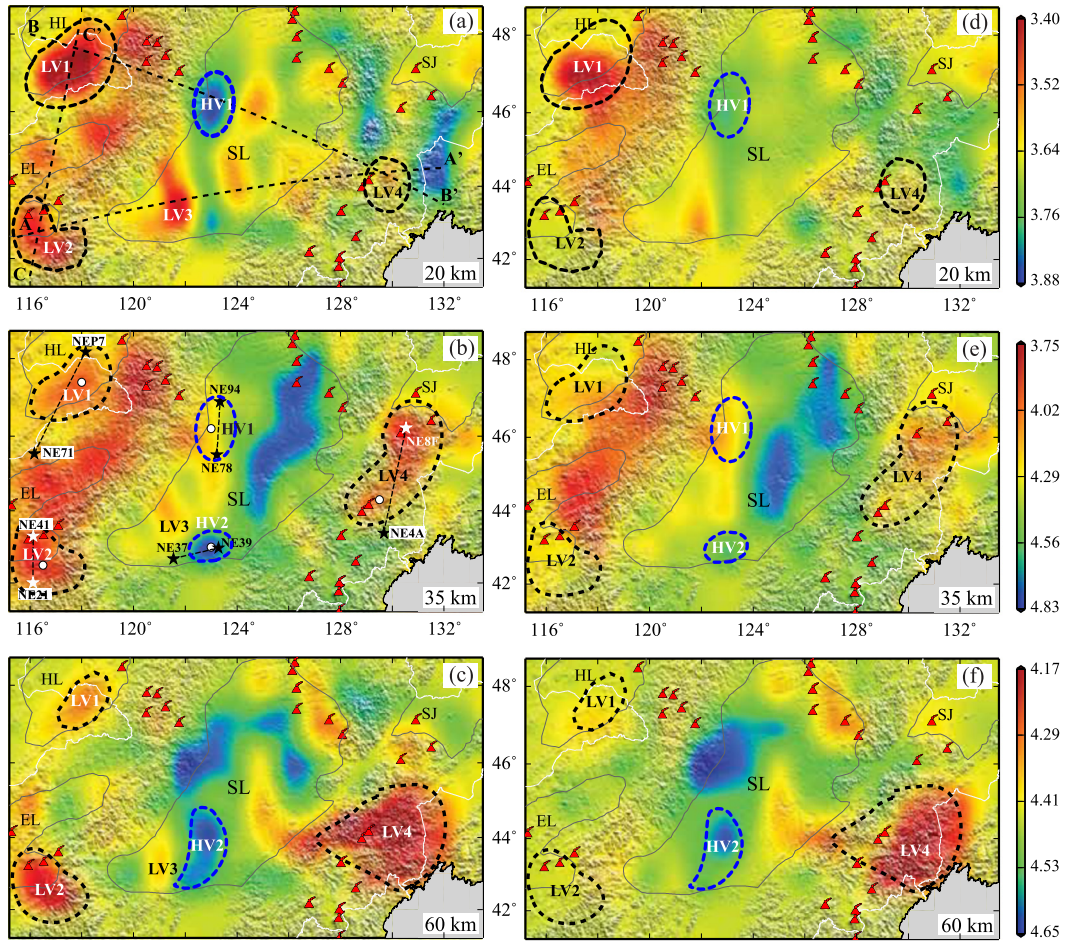


Fig. 4. Shear wave speed maps showing a comparison between the final model (left) and the initial model (right) at three different depths (20 km, 35 km and 60 km). The main differences of the two models are indicated by LVs (low wave speeds) and HVs (high wave speeds).

on the initial model. Therefore, we focus the following discussion based on the S-wave model.

Wave speed distribution of the final S-wave model at three depths, middle crust (20 km), lower crust (35 km) and uppermost mantle (60 km), are shown in Figs. 4a, 4b and 4c, respectively. For comparison, we also show the same depth slices of the initial model from Guo et al. (2015) (Fig. 4, d–f). Although the final model is quite similar to the initial one in most area, the broad crustal LV beneath the Great Xing'an range and large mantle LV beneath the Changbaishan–Jingpohu range in the final model are much stronger than those in the initial model. In addition to these two large-scale LVs, we also find three other medium-sized (~100 km) LVs (LV1, LV2, and LV3), which are not well resolved in the regular surface tomography of Guo et al. (2015, 2016b) (Fig. 4). We attribute the improvements in resolving LVs here to accounting for 3-D propagation effect in adjoint tomography, which is expected to reduce the error caused by wavefront healing. In the following paragraphs, we will focus on the new features revealed by the final model, and discuss their geological implications.

Two strong LVs, labeled as LV1 and LV2, are observed in the northwestern and southwestern corners of the study area, which extend from middle crust to the uppermost mantle. The vertical continuity of these two LVs can be further confirmed from the vertical cross sections that sample the two anomalies (Fig. 5). There is also a strong LV beneath the Quaternary Jingpohu volcanic lake, LV4, which is confined mainly in the lowermost crust and the uppermost mantle depths and changes shape vertically (Figs. 4b and 4c). Beneath the southwestern corner of the Songliao basin, we see a fourth strong LV (LV3) inside the middle crust, with a reduced

intensity in the lower crust and uppermost mantle (Figs. 4a–c and 5a).

The LV1 is located approximately 150 km west to the Halaha volcanic group consisting of 28 Quaternary volcanoes (Figs. 4a–4c). Under the volcanic complex, a moderate LV can be found only at the middle to lower crustal depths (Figs. 4a–4c and 5b). The relative location between the volcanic complex and the LV in the uppermost mantle is consistent with the results of Guo et al. (2016b). We also notice a vertically extending LV at greater than 80 km depths under the volcanic group in their images (Fig. 7a in Guo et al., 2016b). Such a deep LV is likely robust, as the wave speed model obtained by Guo et al. (2016b) is expected to have a decent resolution in the upper mantle depths because both high-frequency ambient noise and low-frequency earthquake data are used in the inversion. Therefore the mantle upwelling associate with the Halaha volcanic group might have drifted westward while it arises from the asthenosphere.

It is worth noting that the shear wave speeds within the LV1 are up to 5.0% lower than that of the initial model (Fig. 6a right). The strong low wave speed is required by the data. The left of Fig. 6a shows the EGFs and the two SGFs computed based on the initial and final models for the station pair NE71–NEP7. Rayleigh waves in the SGFs computed from the initial model, which are shown as the dashed blue lines, arrives systematically earlier than those in the EGFs (solid black lines), while the SGFs based on the final model with a stronger LV match the data much better. In order to better understand the implication of the obtained low wave speeds, we also show the average shear wave speeds of the orogens over the globe together with its uncertainty (green dot-

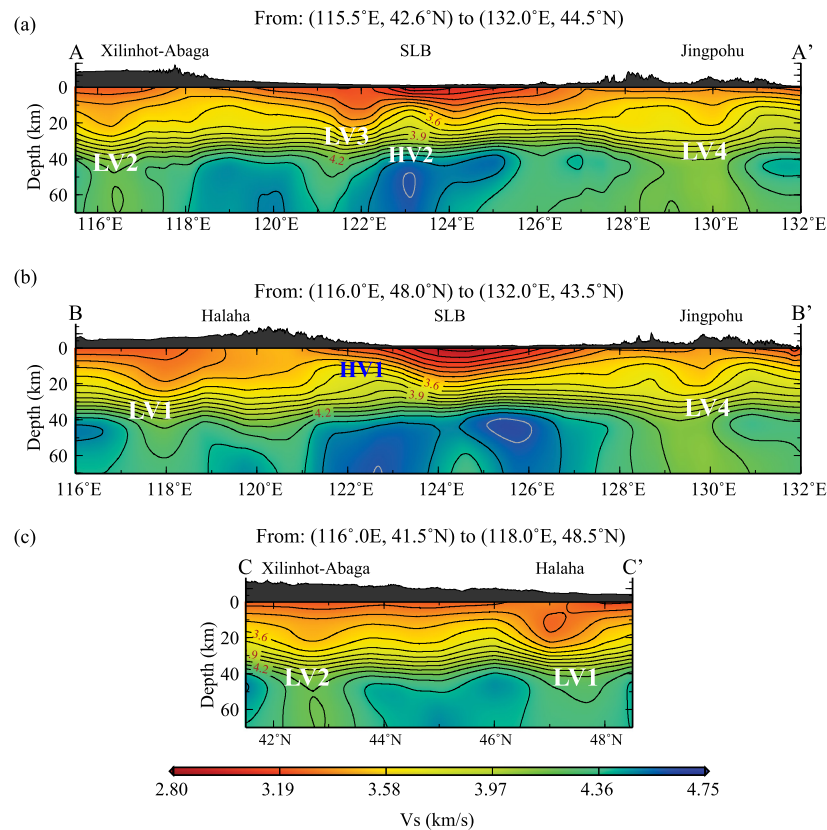


Fig. 5. Cross sections of the final model shear wave speeds along profiles AA', BB', and CC' indicated by black dashed lines in the map of Fig. 4a.

ted line in Fig. 6a right). Both the wave speeds and uncertainties are scaled from the P-wave speed (Christensen and Mooney, 1995) by a factor of 1.732. The crustal thickness beneath all the orogens is 46.3 ± 9.5 km, and the Pn wave speed is 8.01 ± 0.22 km/s (Christensen and Mooney, 1995).

The crustal thickness in the LV1 region is around 35 km, and the underneath mantle has an S_n wave speed of 4.21 km/s. It appears that the S-wave speed inside the LV1 area is even lower than the low-end of the global orogen model in the lower crust and uppermost mantle (Fig. 6a right), indicating that partial melting is likely to exist at these depths. The S-wave speed in the middle and lower crust, as well as the uppermost mantle is $\sim 8.6\%$ lower than the average wave speed, and $\sim 4.5\%$ lower than the low-end S-wave speed of the global orogen model. If we assume that this $\sim 4.5\%$ S-wave speed reduction is caused by partial melting and use a $d \ln V_s / dF$ (partial derivative of S-wave speed with respect to melt fraction) of -5.4 percent per melt fraction (%) (Hammond and Humphreys, 2000), then we obtain a $\sim 1\%$ melt fraction in the mid-to-lower crust and the uppermost mantle. It must be noted that the equation $d \ln V_s / dF = -5.4$ from basaltic rocks under the uppermost mantle pressure–temperature condition, therefore it might be not appropriate to infer melt fraction in the lower crust.

The S-wave speed within LV1 is between 3.33 and 3.61 km/s, which is close to the values obtained by Hacker et al. (2014) for partial melting in crust beneath Central Tibet. Like most of ambient noise tomographic studies (e.g., Guo et al., 2015; Kang et al., 2016), here we do not include azimuthal anisotropy in the inversion, therefore the obtained S-wave speed of LV1, as well as LV2 discussed below, could be biased considering the poor azimuthal coverage of the sampling raypaths. Li and Niu (2010) found that the azimuthal anisotropy within the lithosphere is generally weaker than the global average; we thus expected the effect caused by crustal azimuthal anisotropy is limited.

The medium-sized LV2 is located slightly south to the Xilinhot–Abaga volcanic field, and extends vertically from the middle crust to the uppermost mantle (Figs. 4a–c, and 5a and c). This anomaly seems to extend at least to 200 km based on the joint inversion of Guo et al. (2016b). The LV2, on the other hand, is not well resolved by the regular surface tomography (Fig. 4d–f) (Guo et al., 2015), although it is strongly suggested by the dispersion data that sample the area (Fig. 6b left). The final model shows a shear wave speed reduction from 3.1% to 8.7% in the depth range of 15–70 km as compared to the initial model (Fig. 6b right). The absolute wave speeds inside the lower crust and upper mantle are also below the low ends of the global orogen model, and are comparable to those in the LV1 region, suggesting the presence of $\sim 1\%$ partial melts at these depths, which are the likely source that feeds the Xilinhot–Abaga volcanoes.

We further speculate that the two strong low velocity anomalies in the lower crust beneath the two Cenozoic volcanic complexes are likely intruded basaltic magma bodies, just like the one beneath the Yellowstone supervolcano proposed by Huang et al. (2015). As mentioned above, geochemistry studies suggested that the alkaline basalts from the two Cenozoic volcanic complexes have a deep origin in the asthenosphere; therefore the basaltic lower crustal magma bodies act as bridges, linking the shallow magma reservoirs with the upper mantle upwellings.

The LV3 anomaly inside the southwestern margin of the Songliao basin (Fig. 4a–c) is the smallest one among the three anomalies, and is also not shown clearly in the initial model. It has the largest wave speed reduction at the middle crustal depths (Fig. 4a) and then fades gradually with increasing depth (Figs. 4b and 4c). The vertically extending anomaly is, however, still recognizable from the depth section of wave speed distribution (Fig. 5a). The moderate amplitude of the anomaly in the lower crust and uppermost mantle depths might explain the lack of surface magmatism right above the LV3.

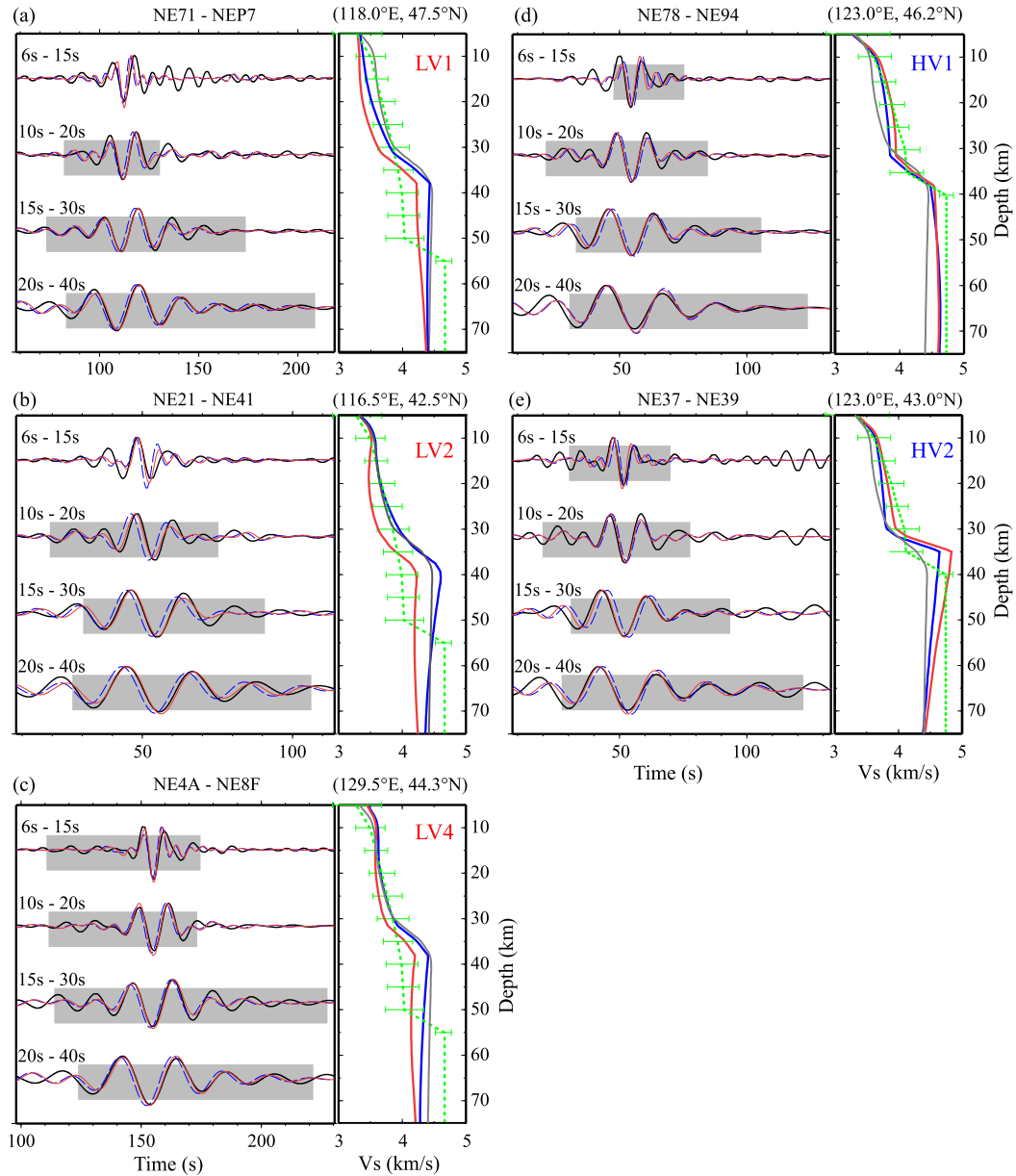


Fig. 6. (a) Left of each panel: The EGF (black solid line) from a station pair NE71–NEP7 that samples the LV1 anomaly is shown together with the SGFs of the initial (blue dashed line) and final (red solid line) models, respectively. The EGF and SGFs are filtered in four period bands: 6–15 s, 10–20 s, 15–30 s, and 20–40 s, which are plotted from the top to the bottom. The locations of NE71 and NEP7 are shown in Fig. 4b. Right: Shear wave speed profile of the final model (red solid line) at the grid (118.0°E, 47.5°N) inside the LV1 anomaly is plotted together with the initial (blue solid line), regional average (gray solid line), and global model (green dashed lines) for comparison. The horizontal bars on the green lines represent the range of velocity variations beneath different types of continental crust, for example orogens, rifts, extended crusts, etc. (Christensen and Mooney, 1995). The geographic location of the grid is marked as white dot in Fig. 4b. (b) Same as (a), except for LV2. (c) Same as (a), except for LV4. (d) Same as (a), except for HV1. (e) Same as (a), except for HV2. The global orogen model is used in (a–c) and the extended crust model is used in (d) and (e). (For interpretation of the references to color in this figure legend, the reader is referred to the web version of this article.)

We also find a strong LV in the eastern margin of the Songliao basin, the LV4, located in the Jingpohu volcanic lake area. This anomaly has almost a normal shear wave speed in the middle crust in both the initial and final models (Fig. 4a and 4d). Wave speed reduction becomes significant in the lower crust (Figs. 4b and 4e), and reaches the maximum in the uppermost mantle (Fig. 4c and 4f). The final S-wave speeds in the lower crust and the uppermost mantle are, respectively, 2.8% and 4.7% lower than the initial values. These changes in wave speeds seem to be required by the data (Fig. 6c left). The final wave speeds (red solid line in Fig. 6c right) lie in the range of wave speeds observed beneath different orogens around the world (green dotted line with error bars in Fig. 6c right).

It is worth noting here that the strong LV beneath the Changbaishan volcanic complex revealed by the body wave tomography (Tang et al., 2014) and joint inversion of EGFs and teleseismic surface wave data (Guo et al., 2016b) is not shown in our model. This is because the interstation ray paths from the station distribution shown in Fig. 1 do not sample the volcanic complex, and therefore the ambient noise data of the 127 stations alone do not have the ability to resolve wave speed structure beneath the volcanic complex.

Using the receiver function data from the NECESSArray stations, Tao et al. (2014) measure the Moho depth and compute the corresponding Airy isostasy topography of the study area. They further compute the residual topography by taking the difference

between the observed and Airy isostasy topography. A positive residual means that the higher-than-expected elevation might have been supported dynamically. They find a good spatial correlation between the positive residual topography and distribution of Quaternary volcanoes along the eastern margin of the Songliao basin, which is consistent with a scenario for a mantle upwelling that dynamically supports part of the elevation. We find that the LV1 and LV2 associated with the Halaha and Xilinhote–Abaga volcanic complexes are also located inside areas with positive residual topography.

In addition to the LV1 and LV2 anomalies in the Great Xing'an range, the LV3 inside the Songliao basin is also located at a broad area with positive residual topography that covers a large part of the southern Songliao basin. Li et al. (2016) find that the low wave speed sediments beneath the Songliao basin extends to ~2–3 km deep in the south and ~5–6 km in the north, mainly due to the insignificant postrift subsidence in the south (Wei et al., 2010). Thus we argue that LV3 is likely the dynamic source for the positive residual topography and the minor postrift subsidence observed at the southwestern Songliao basin.

In addition to the LVs with enhanced wave speed reduction, we also find two high wave speed anomalies located in the west (HV1) and south (HV2) sides of the Songliao basin. The HV1 has a middle crustal component (Fig. 4a), which is not present in the initial model (Fig. 4d) but is required by the data (Fig. 6d left). The S-wave speeds of the final model are ~0.32–2.65% higher than the initial values in the crust, and are comparable to those in the initial model in the mantle. Both are within the wave speed range of the global model for extended crust (Fig. 5d right). The HV2 anomaly is essentially located inside the mantle (Fig. 5a), and is well supported by the data (Fig. 6e left). It has an Sn wave speed slightly higher than the global average for extended crust (Fig. 6e right). Both HV1 and HV2 are parts of the large-scale high wave speed mantle anomaly beneath the western edge of the Songliao basin, which is interpreted by Guo et al. (2016b) as the downwelling part of the convection cell beneath NE China. The Xilinhote–Abaga and the Halaha volcanic groups located at the Great Xing'an range further west are originated from upward return flows of the above downwelling (Guo et al., 2016b).

5. Conclusions

We conduct a SEM based adjoint tomography with ambient noise data recorded by the broadband NECESSArray in NE China. Compared to the 3-D model inverted with the regular surface tomography based on great circle raypath approximation and 1-D dispersion matching, our model reveals the following new features on shear wave speed structure of the crust and uppermost mantle beneath the area: (1) below the Xilinhote–Abaga and Halaha volcanic complexes, there is a vertically extending low wave speed body inside the lower crust and uppermost mantle, which shows a wave speed reduction indicative of partial melting; (2) a mantle upwelling is observed beneath the southwestern part of the Songliao basin, which may explain the observed dynamic topography and low postrift subsidence of the area; (3) the broad low wave speed anomaly beneath the Great Xing'an range lies mainly inside the lower crust, while the broad swell around the Jingpohu lake is mainly supported by a low wave speed anomaly in the upper mantle. Since it better accounts for the finite-frequency kernels in 3-D space, the adjoint tomography offers a promising way to recover more adequate amplitude of velocities anomalies as compared to the traditional surface wave tomography.

Acknowledgements

We thank all the people involved in the NECESSArray project for installing and servicing the seismic array. We thank Dr. Z. Guo for providing the ambient noise data and his 3-D model. We also thank all members in the Rice Research Computing Support Group and the staff members of the Extreme Science and Engineering Discovery Environment (XSEDE) for their technical help, and two anonymous reviewers for their constructive comments and suggestions, which significantly improved the quality of this paper. This work is supported by NSF grants EAR-1345096, EAR-1547228, and NSFC grant 41274099; YL is supported by the China Scholarship Council under grant 201406400022 and the Open Fund No. GDL1506 of the Key Laboratory of Geo-Detection, China University of Geosciences, Beijing. XSEDE is supported by NSF ACI-1053575.

References

- Bensen, G.D., Ritzwoller, M.H., Barmin, M.P., Levshin, A.L., Lin, F., Moschetti, M.P., Shapiro, N.M., Yang, Y., 2007. Processing seismic ambient noise data to obtain reliable broad-band surface wave dispersion measurements. *Geophys. J. Int.* 169, 1239–1260. <http://dx.doi.org/10.1111/j.1365-246X.2007.03374.x>.
- Chen, M., Huang, H., Yao, H., van der Hilst, R.D., Niu, F., 2014. Low wave speed zones in the crust beneath SE Tibet revealed by ambient noise adjoint tomography. *Geophys. Res. Lett.* 41, 334–340. <http://dx.doi.org/10.1002/2013GL058466>.
- Chen, S.S., Fan, Q.C., Zou, H.B., Zhao, Y.W., Shi, R.D., 2015. Geochemical and Sr–Nd isotopic constraints on the petrogenesis of late Cenozoic basalts from the Abaga area, Inner Mongolia, eastern China. *J. Volcanol. Geotherm. Res.* 305, 30–44. <http://dx.doi.org/10.1016/j.jvolgeores.2015.09.018>.
- Christensen, N.I., Mooney, W.D., 1995. Seismic velocity structure and composition of the continental crust: a global view. *J. Geophys. Res.* 100, 9761–9788. <http://dx.doi.org/10.1029/95JB00259>.
- Eizenhöfer, P.R., Zhao, G., Zhang, J., Sun, M., 2014. Final closure of the Paleo-Asian Ocean along the Solonker Suture Zone: constraints from geochronological and geochemical data of Permian volcanic and sedimentary rocks. *Tectonics* 33, 441–463. <http://dx.doi.org/10.1002/2013TC003357>.
- Fan, Q., Zhao, Y., Chen, S., Li, N., Sui, J., 2015. Quaternary volcanic activities in the West of Daxing'anling–Taihangshan Gravity Lineament. *Bull. Miner., Petrol. Geochem.* 4, 674–681. <http://dx.doi.org/10.3969/j.issn.1007-2802.2015.04.001>.
- Feng, Z., Jia, C., Xie, X., Zhang, S., Feng, Z., Cross, T.A., 2010. Tectonostratigraphic units and stratigraphic sequences of the nonmarine Songliao basin, northeast China. *Basin Res.* 22, 79–95. <http://dx.doi.org/10.1111/j.1365-2117.2009.00445.x>.
- Ge, R., Zhang, Q., Wang, S., Xue, A., Xu, S., Chen, J., Xiyong, W., 2010. Tectonic evolution of Songliao Basin and the Prominent Tectonic Regime Transition in Eastern China. *Geol. Rev.* 56, 180–195.
- Guo, P., Niu, Y., Sun, P., Ye, L., Liu, J., Zhang, Y., Feng, Y., Zhao, J., 2016a. The origin of Cenozoic basalts from central Inner Mongolia, East China: the consequence of recent mantle metasomatism genetically associated with seismically observed paleo-Pacific slab in the mantle transition zone. *Lithos* 240–243, 104–118. <http://dx.doi.org/10.1016/j.lithos.2015.11.010>.
- Guo, Z., Chen, Y.J., Ning, J., Feng, Y., Grand, S.P., Niu, F., Kawakatsu, H., Tanaka, S., Obayashi, M., Ni, J., 2015. High resolution 3-D crustal structure beneath NE China from joint inversion of ambient noise and receiver functions using NECESSArray data. *Earth Planet. Sci. Lett.* 416, 1–11. <http://dx.doi.org/10.1016/j.epsl.2015.01.044>.
- Guo, Z., Chen, Y.J., Ning, J., Yang, Y., Afonso, J.C., Tang, Y., 2016b. Seismic evidence of on-going sublithosphere upper mantle convection for intra-plate volcanism in Northeast China. *Earth Planet. Sci. Lett.* 433, 31–43. <http://dx.doi.org/10.1016/j.epsl.2015.09.035>.
- Hacker, B.R., Ritzwoller, M.H., Xie, J., 2014. Partially melted, micabearing crust in Central Tibet. *Tectonics* 33. <http://dx.doi.org/10.1002/2014TC003545>.
- Hammond, W.C., Humphreys, E.D., 2000. Upper mantle seismic wave attenuation: effects of realistic partial melt distribution. *J. Geophys. Res.* 105, 10987–10999. <http://dx.doi.org/10.1029/2000jb900042>.
- Harmon, N., Rychert, C., Gerstoft, P., 2010. Distribution of noise sources for seismic interferometry. *Geophys. J. Int.* 183, 1470–1484. <http://dx.doi.org/10.1111/j.1365-246X.2010.04802.x>.
- Hu, W., Cai, C., Wu, Z., Li, J., 1998. Structural style and its relation to hydrocarbon exploration in the Songliao Basin, northeast China. *Mar. Pet. Geol.* 15, 41–55. [http://dx.doi.org/10.1016/S0264-8172\(97\)00054-8](http://dx.doi.org/10.1016/S0264-8172(97)00054-8).
- Huang, H.-H., Lin, F., Schmandt, B., Farrell, J., Smith, R.B., Tsai, V.C., 2015. The Yellowstone magmatic system from the mantle plume to the upper crust. *Science* 348, 773–776. <http://dx.doi.org/10.1126/science.1256484>.
- Hung, S.-H., Dahlen, F.A., Nolet, G., 2001. Wavefront healing: a banana-doughnut perspective. *Geophys. J. Int.* 146, 289–312.

- Kang, D., Shen, W., Ning, J., Ritzwoller, M.H., 2016. Seismic evidence for lithospheric modification associated with intracontinental volcanism in Northeastern China. *Geophys. J. Int.* 204, 215–235.
- Klimetz, M.P., 1983. Speculations on the Mesozoic Plate tectonic evolution of eastern China. *Tectonics* 2, 139–166. <http://dx.doi.org/10.1029/TC002i002p00139>.
- Komatitsch, D., Liu, Q., Tromp, J., Süß, P., Stidham, C., Shaw, J.H., 2004. Simulations of ground motion in the Los Angeles Basin based upon the spectral-element method. *Bull. Seismol. Soc. Am.* 94, 187–206. <http://dx.doi.org/10.1785/0120030077>.
- Komatitsch, D., Tromp, J., 2002a. Spectral-element simulations of global seismic wave propagation—I: validation. *Geophys. J. Int.* 149, 390–412. <http://dx.doi.org/10.1046/j.1365-246X.2002.01653.x>.
- Komatitsch, D., Tromp, J., 2002b. Spectral-element simulations of global seismic wave propagation—II: three-dimensional models, oceans, rotation and self-gravitation. *Geophys. J. Int.* 150, 303–318. <http://dx.doi.org/10.1046/j.1365-246X.2002.01716.x>.
- Lei, J., Zhao, D., 2005. P-wave tomography and origin of the Changbai intraplate volcano in Northeast Asia. *Tectonophysics* 397, 281–295. <http://dx.doi.org/10.1016/j.tecto.2004.12.009>.
- Li, G., Chen, H., Niu, F., Guo, Z., Yang, Y., Xie, J., 2016. Measurement of Rayleigh wave ellipticity and its application to the joint inversion of high-resolution S wave velocity structure beneath northeast China. *J. Geophys. Res., Solid Earth* 121, 864–880. <http://dx.doi.org/10.1002/2015JB012459>.
- Li, J., Niu, F., 2010. Seismic anisotropy and mantle flow beneath northeast China inferred from regional seismic networks. *J. Geophys. Res.* 115, B12327. <http://dx.doi.org/10.1029/2010JB007470>.
- Li, J.-Y., 2006. Permian geodynamic setting of Northeast China and adjacent regions: closure of the Paleo-Asian Ocean and subduction of the Paleo-Pacific Plate. *J. Asian Earth Sci.* 26, 207–224. <http://dx.doi.org/10.1016/j.jseae.2005.09.001>.
- Li, S., Ouyang, Z., 1998. Tectonic framework and evolution of Xing'anling–Mongolian orogenic belt (XMOB) and its adjacent region. *Mar. Geol. Quat. Geol.* 18, 46–55.
- Li, S., Chen, F., Siebel, W., Wu, J., Zhu, X., Shan, X., Sun, X., 2012. Late Mesozoic tectonic evolution of the Songliao basin, NE China: evidence from detrital zircon ages and Sr–Nd isotopes. *Gondwana Res.* 22, 943–955. <http://dx.doi.org/10.1016/j.gr.2012.04.002>.
- Lin, Z., 2011. Characteristics of Tancheng–Lujiang fault and its role on basin controlling. *J. Geomech.* 17, 322–327. <http://dx.doi.org/10.3969/j.issn.1006-6616.2011.04.003>.
- Liu, J., Han, J., Fyfe, W.S., 2001. Cenozoic episodic volcanism and continental rifting in northeast China and possible link to Japan Sea development as revealed from K–Ar geochronology. *Tectonophysics* 339, 385–401. [http://dx.doi.org/10.1016/S0040-1951\(01\)00132-9](http://dx.doi.org/10.1016/S0040-1951(01)00132-9).
- Luo, Y., 2012. Seismic Imaging and Inversion Based on Spectral-Element and Adjoint Methods. Ph.D. thesis. Dept. of Geosciences, Princeton Univ., Princeton, USA.
- Maggi, A., Tape, C., Chen, M., Chao, D., Tromp, J., 2009. An automated time-window selection algorithm for seismic tomography. *Geophys. J. Int.* 178, 257–281. <http://dx.doi.org/10.1111/j.1365-246X.2009.04099.x>.
- Malcolm, A.E., Trampert, J., 2011. Tomographic errors from wave front healing: more than just a fast bias. *Geophys. J. Int.* 185, 385–402. <http://dx.doi.org/10.1111/j.1365-246X.2011.04945.x>.
- Meng, Q.-R., 2003. What drove late Mesozoic extension of the northern China–Mongolia tract? *Tectonophysics* 369, 155–174. [http://dx.doi.org/10.1016/S0040-1951\(03\)00195-1](http://dx.doi.org/10.1016/S0040-1951(03)00195-1).
- Panning, M., Romanowicz, B., 2006. A three-dimensional radially anisotropic model of shear velocity in the whole mantle. *Geophys. J. Int.* 167, 361–379. <http://dx.doi.org/10.1111/j.1365-246X.2006.03100.x>.
- Roux, P., Sabra, K.G., Kuperman, W.A., Roux, A., 2005. Ambient noise cross correlation in free space: theoretical approach. *J. Acoust. Soc. Am.* 117, 79–84. <http://dx.doi.org/10.1121/1.1830673>.
- Shao, J., Zang, S., Mou, B., Li, X., Wang, B., 1994. Orogenic belt extensional tectonic and asthenosphere uplift – a case study of Xingmeng Orogen. *Chin. Sci. Bull.* 39, 533–537.
- Tang, Y., Obayashi, M., Niu, F., Grand, S.P., Chen, Y.J., Kawakatsu, H., Tanaka, S., Ning, J., Ni, J.F., 2014. Changbaishan volcanism in northeast China linked to subduction-induced mantle upwelling. *Nat. Geosci.* 7, 470–475. <http://dx.doi.org/10.1038/ngeo2166>.
- Tao, K., Niu, F., Ning, J., Chen, Y.J., Grand, S., Kawakatsu, H., Tanaka, S., Obayashi, M., Ni, J., 2014. Crustal structure beneath NE China imaged by NECESSArray receiver function data. *Earth Planet. Sci. Lett.* 398, 48–57. <http://dx.doi.org/10.1016/j.epsl.2014.04.043>.
- Tromp, J., Tape, C., Liu, Q., 2005. Seismic tomography, adjoint methods, time reversal and banana-doughnut kernels. *Geophys. J. Int.* 160, 195–216. <http://dx.doi.org/10.1111/j.1365-246X.2004.02453.x>.
- Van der Voo, R., van Hinsbergen, D.J.J., Domeier, M., Spakman, W., Torsvik, T.H., 2015. Latest Jurassic–earliest Cretaceous closure of the Mongol–Okhotsk Ocean: a paleomagnetic and seismological–tomographic analysis. *Spec. Pap., Geol. Assoc. Can.* 513. [http://dx.doi.org/10.1130/2015.2513\(19\)](http://dx.doi.org/10.1130/2015.2513(19)).
- Wang, F., Zhou, X., Zhang, L., Ying, J., Zhang, Y., Wu, F., Zhu, R., 2006. Late Mesozoic volcanism in the Great Xing'an Range (NE China): timing and implications for the dynamic setting of NE Asia. *Earth Planet. Sci. Lett.* 251, 179–198. <http://dx.doi.org/10.1016/j.epsl.2006.09.007>.
- Wang, Y., Li, C., Wei, H., Shan, X., 2003. Late Pliocene–recent tectonic setting for the Tianchi volcanic zone, Changbai Mountains, northeast China. *J. Asian Earth Sci.* 21, 1159–1170. [http://dx.doi.org/10.1016/S1367-9120\(03\)00019-1](http://dx.doi.org/10.1016/S1367-9120(03)00019-1).
- Weaver, R.L., Lobkis, O.I., 2004. Diffuse fields in open systems and the emergence of the Green's function (L). *J. Acoust. Soc. Am.* 116, 2731. <http://dx.doi.org/10.1121/1.1810232>.
- Wei, H., Liu, J., Meng, Q., 2010. Structural and sedimentary evolution of the southern Songliao Basin, northeast China, and implications for hydrocarbon prospectivity. *Am. Assoc. Pet. Geol. Bull.* 94, 531–564. <http://dx.doi.org/10.1306/09080909060>.
- Wilhem, C., Windley, B.F., Stampfli, G.M., 2012. The Altaids of Central Asia: a tectonic and evolutionary innovative review. *Earth-Sci. Rev.* 113, 303–341. <http://dx.doi.org/10.1016/j.earscirev.2012.04.001>.
- Xing, X., Niu, F., Chen, M., Yang, Y., 2016. Effects of shallow density structure on the inversion for crustal shear wavespeeds in surface wave tomography. *Geophys. J. Int.* 205, 1144–1152. <http://dx.doi.org/10.1093/gji/ggw064>.
- Xu, Y., 2006. Formation of the Taihangshan gravity lineament by the diachronous lithospheric thinning of the North China Craton. *Earth Sci., J. China Univ. Geosci.* 31.
- Yao, H., van der Hilst, R.D., 2009. Analysis of ambient noise energy distribution and phase velocity bias in ambient noise tomography, with application to SE Tibet. *Geophys. J. Int.* 179, 1113–1132. <http://dx.doi.org/10.1111/j.1365-246X.2009.04329.x>.
- Zhao, W., Zou, C., Feng, Z., Hu, S., Zhang, Y., Li, M., Wang, Y., Yang, T., Yang, H., 2008. Geological features and evaluation techniques of deep-seated volcanics gas reservoirs, Songliao Basin. *Pet. Explor. Dev.* 35, 129–142. [http://dx.doi.org/10.1016/S1876-3804\(08\)60019-1](http://dx.doi.org/10.1016/S1876-3804(08)60019-1).
- Zhou, J., Wilde, S.A., 2013. The crustal accretion history and tectonic evolution of the NE China segment of the Central Asian Orogenic Belt. *Gondwana Res.* 23, 1365–1377. <http://dx.doi.org/10.1016/j.gr.2012.05.012>.
- Zhou, Y., Dahlen, F.A., Nolet, G., 2004. Three-dimensional sensitivity kernels for surface wave observables. *Geophys. J. Int.* 158, 142–168. <http://dx.doi.org/10.1111/j.1365-246X.2004.02324.x>.
- Zou, H., Fan, Q., Yao, Y., 2008. U–Th systematics of dispersed young volcanoes in NE China: asthenosphere upwelling caused by piling up and upward thickening of stagnant Pacific slab. *Chem. Geol.* 255, 134–142. <http://dx.doi.org/10.1016/j.chemgeo.2008.06.022>.